Radiation damage at the aluminum entrance window of the SINQ Target 3

W. Lu [a], M.S. Wechsler [a,*], Y. Dai [b]

[a] *Department of Nuclear Engineering, North Carolina State University, Raleigh, NC 27695-7909, USA*
[b] *Spallation Source Division, Paul Scherrer Institute, CH-5232 Villigen PSI, Switzerland*

Abstract

Calculations are underway to determine radiation damage (displacement, helium, and hydrogen production) at the entrance window of the SINQ Target 3 (Mark II Type). Damage production rates were determined in two ways. In Method 1, the displacement, He, and H cross-sections were folded into the proton and neutron fluxes to give the three defect production rates separately for protons and neutrons. In Method 2, MCNPX with a computer model of SINQ was used directly to calculate the three production rates due to the combined effects of protons and neutrons. The production rates at the central tip of the target by Method 1 are 4.1 and 0.47 dpa/yr per mA for protons and neutrons, respectively, giving a total of 4.6 dpa/yr per mA. By Method 2 using several approaches, we obtain a range of production rates from 3.6 to 4.1 dpa/yr per mA. For helium, the production rates are calculated to be about 1000 and a range from 950 to 1580 appmHe/yr per mA, respectively. LAHET calculations indicate that the helium is completely retained in the irradiated aluminum. For hydrogen, the calculations indicate that perhaps only about half of the hydrogen produced is retained. Method 1 gives about 3500 appmH/yr per mA retained and Method 2 gives a range from 3500 to 4400 appmH/yr per mA.
© 2003 Elsevier Science B.V. All rights reserved.

1. Introduction

The targets at the SINQ facility at the Paul Scherrer Institute receive a continuous beam of protons from an isochronous ring-cyclotron at an energy of about 570 MeV. The SINQ Target 3 (Mark II Type) operated during 1998 and 1999 under the first experiment of the SINQ Target Irradiation Program, STIP-I. In this experiment, more than 1500 sub-size samples were irradiated, receiving a total proton charge of 6.77 Ah with a peak fluence of 3.2×10^{25} p/m^2 [1,2]. The total beam current was about 0.86 mA, as shown in Fig. 10 of [1]. Included among the samples were 40 different types of materials for tensile, bend-fatigue, tear, bend-bar,

Charpy, shear punch, and transmission-electron-microscopy testing (Table 1 in [1]). The purpose of the present paper is to describe calculations of the radiation damage (displacement, helium, and hydrogen production) at the entrance window of the SINQ Target 3 that took place during the STIP-I experiment.

Fig. 1 gives a sketch of the lower part of Target 3. The filled circles represent Zircaloy-2 target rods, the circles with number or letter designations represent Zircaloy tubes containing mechanical-property and TEM samples or filler metals, and the empty circles represent empty Zircaloy tubes. The two container shells are made of an aluminum-2.7 wt% magnesium alloy. The shells are 3-mm thick, and they are separated by a 4-mm gap containing flowing D$_2$O coolant. D$_2$O coolant also flows downward adjacent to the inner wall of the inner shell and then upward past the Zircaloy rods and tubes. The specific contents of the tubes are given in Table 3 of [1]. The entrance window is the hemispherical cap at the bottom of the target shown in Fig. 1. The

* Corresponding author. Present address: 106 Hunter Hill Place, Chapel Hill, NC 27517-9128, USA. Tel.: +1-919 929 5193; fax: +1-919 933 6727.
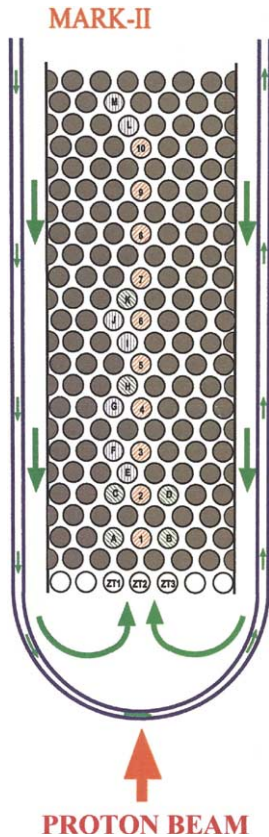 *E-mail address:* wechsler@ncsu.edu (M.S. Wechsler).

Fig. 1. SINQ Target 3 (Mark II Type). Note that there are actually nine or ten rods in each layer (see, [1], Fig. 7).
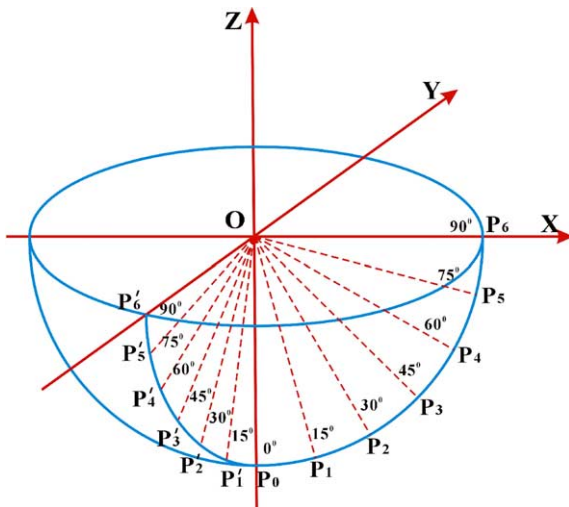
upward (in what follows, in the Z direction). The main focus of this paper is to present calculations of radiation damage at the downward tip of the target and at neighboring points in the hemispherical region. Fig. 2 shows the calculation points for the entrance window. The main emphasis is on the tip of the window at point P_0. The X direction is along the axis of the rods and tubes.

2. Incident proton beam

Our calculations were greatly aided by the LAHET [3] input file modeling the SINQ Target 3 (Mark II Type) target prepared by Pepin [4]. In accord with [4], we consider the incident proton beam to have a double-Gaussian current density profile over an ellipse and zero current density outside of the ellipse, consistent with option ISOPT = 2 in the LAHET input file. In this case, the current density function is given by

$$\frac{p(x,y)}{p(0,0)} = \exp\left\{ -(1/2)\left[\left(\frac{x}{a}\right)^2 + \left(\frac{y}{b}\right)^2\right]\right\}, \tag{1}$$

where the beam is in the Z direction and the ellipse is in the X–Y plane. In (1), $p(x,y)$ is such that $p(x,y)\,dx\,dy$ is proportional to the proton current flowing between x and $x + dx$ and between y and $y + dy$. In the input file, one chooses values for a and b, which are then the Gaussian parameters σ_x and σ_y, respectively. Pepin chose the values $a = \sigma_x = 3.56$ cm and $b = \sigma_y = 2.12$ cm. Pepin also chose the semi-major and semi-minor axes of the ellipse to be $2a = 7.12$ cm and $2b = 4.24$ cm,
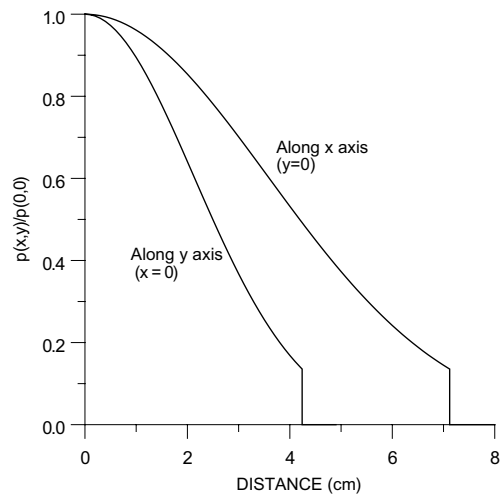

Fig. 2. Calculation points for the entrance window.

Fig. 3. Proton source profile. $p(x,y)$ is the current density function in the plane perpendicular to the beam direction. Double Gaussian with sigma-$x = a = 3.56$ cm and sigma-$y = b = 2.12$ cm. Cutoff parameter $= c = 2$.

diameter of the outer surface of the outer shell is 21.2 cm. As shown in Fig. 1, the proton beam direction is

which corresponds to a cutoff parameter of $c = 2$ [3]. Fig. 3 shows a plot of $p(x, y)/p(0, 0)$ verus x and y, and the cutoffs at 7.12 and 4.24 cm are clearly seen.

3. Proton and neutron fluxes

For calculating proton and neutron fluxes we ran MCNPX [5], which consists of a merger of MCNP [6] and LAHET [3]. The number of histories was one million. Track-length tallies were conducted at a series of calculation points shown in Fig. 2. P_0 is the lowest point on the Z-axis of the entrance window. In addition, there are six calculation points in the XZ plane (P_1 to P_6) and six calculation points in the YZ plane (P'_1 to P'_6). The radius vectors, OP_1 and OP'_1, make deviation angles with the $-Z$ direction of 15°, OP_2 and OP'_2 make deviation angles of 30°, and so on until OP_6 and OP'_6 make deviation angles of 90° with the $-Z$ direction. The tally volume for points P_6 and P'_6 was 0.0353 cm^3; for all the other points it was 0.0706 cm^3. The total proton flux is shown in Fig. 4 as a function of deviation angle for points in the XZ and YZ planes. Consistent with the proton source profile in Fig. 3, the total proton flux in Fig. 4 decreases more rapidly with increasing deviation angle for points in the YZ plane than for points in the XZ plane. The peak proton flux at the tip of the entrance window (point P_0 at zero deviation angle) is 1.56×10^{14} protons/cm^{2}s per mA, and for the current of 0.86 mA it is 1.34×10^{14} protons/cm^{2}s.

Fig. 5 shows the differential proton flux at the tip of the entrance window as a function of proton energy. As can be clearly seen, the proton energy distribution is strongly dominated by the incident proton beam energy of 570 MeV. In fact, analysis of the data reveals that
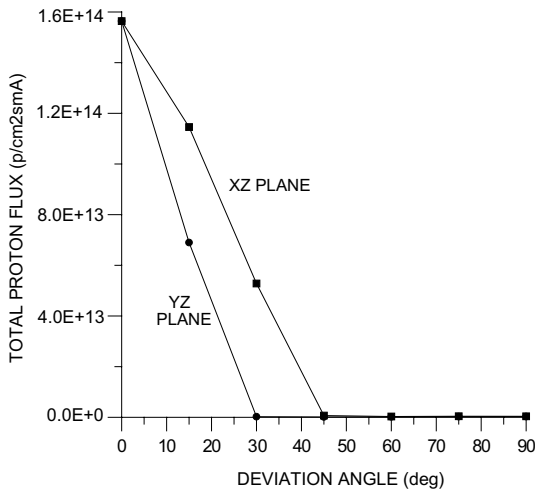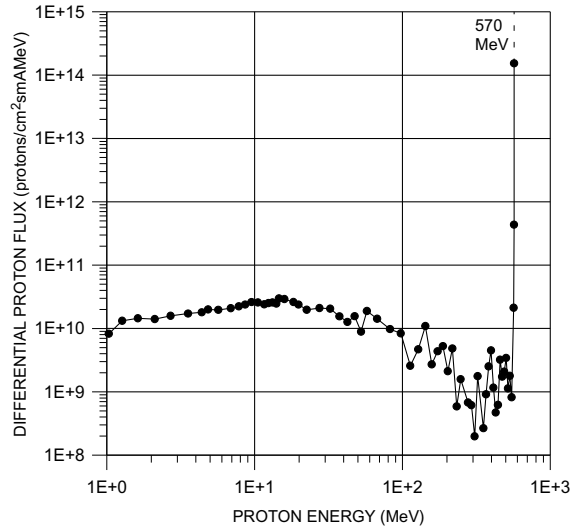

Fig. 5. Differential proton flux versus proton energy for the on-axis tip of the SINQ Target 3 entrance window.
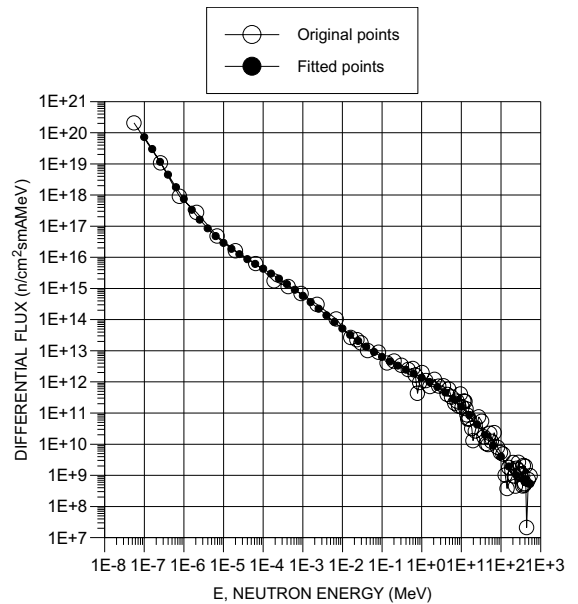

Fig. 6. Differential neutron flux versus neutron energy for the entrance window of SINQ (aluminum, on-axis). Original SINQ differential neutron flux points and points fitted to a 7th-order polynomial.

Fig. 4. Total proton flux versus deviation angle for calculation points in the XZ and YZ planes.

more than 98% of the protons in the flux at the center of the entrance window have energies between 569 and 570 MeV. Thus, secondary protons comprise less than 2% of the proton flux. It follows that the production of displacements, helium, and hydrogen due to protons at the tip of the window may be calculated reasonably
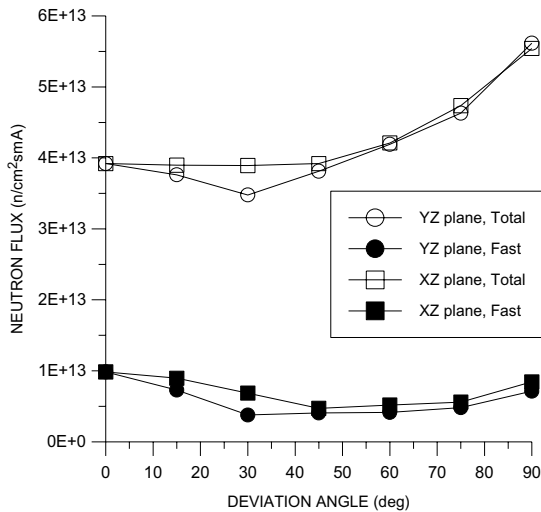
Fig. 7. Total and fast ($E > 0.1$ MeV) neutron flux versus deviation angle for calculation points in the *YZ* and *XZ* planes.

accurately by assuming that all of the protons have the incident energy of 570 MeV.

The energy distribution at the tip of the entrance window of the neutron flux is quite different than that for the proton flux, as can be seen in Fig. 6. The differential neutron flux increases with decreasing neutron energy. The original calculated points are shown as open circles. To facilitate additional analysis, the original points were fitted by a seventh-order least-squares ln–ln fit. The fitted points (filled circles) are located at equal intervals on a lnE scale with five points per energy decade.

The total and fast ($E > 0.1$ MeV) neutron fluxes are plotted in Fig. 7 as a function of the deviation angle from the $-Z$ direction for the calculation points in the *XZ* and *YZ* planes indicated in Fig. 2. The fast fluxes stay fairly constant as a function of deviation angle, whereas the total fluxes increase somewhat at the deviation angles above about 45°.

4. Cross-sections and damage rates

4.1. Methods of calculation; methods 1 and 2

In Method 1 cross-sections for displacement, helium, and hydrogen are determined first. In the past, we used SPECTER [8] and LAHET [3] for calculating cross-sections for energies below and above 20 MeV, respectively. The SPECTER code deals with neutron projectiles only and the underlying cross-sections stem from the ENDF libraries. It has been observed for a variety of target materials [9–17], however, that LAHET

consistently underpredicts the neutron displacement cross-section at 20 MeV in comparison to cross-sections obtained from SPECTER. Since the SPECTER cross-sections stem from evaluated nuclear information whereas the LAHET results depend upon models that are generally regarded as questionable below 150 or 200 MeV, more credence can be placed on the SPECTER values. More recently, this problem of the SPECTER-LAHET discrepancy near 20 MeV has been reduced due to the availability of the LA150 neutron and proton cross-section library, which extends up to 150 MeV [18]. Much of the data in the LA150 compilations are generated using the GNASH code [19], although the results are validated with comparisons with experiment where available. The improvement that is realized by using SPECTER below 20 MeV, LA150 from 20 to 150 MeV, and LAHET above 150 MeV is illustrated by neutrons on 316 stainless steel (316SS). For this case, it was found that at 20 MeV the displacement cross-section from SPECTER is about 1000 barns higher than the LAHET cross-section, whereas at 150 MeV the LA150 cross-section is only about 290 barns above the LAHET value [17]. Also, at 20 Mev SPECTER and LA150 are in essential agreement [17]. In running LAHET in order to obtain the cross-sections with Method 1, a synthetic sample is assumed (usually a right-circular cylinder with thickness in the beam direction of about 0.1 to 2 cm). The cross-sections and fluxes, each as a function of energy with the same energy bin structure, are then folded together to yield the damage production rates as a function of energy. When a SPECTER/LA150/LAHET cross-section set was used for neutrons on aluminum at SNS, 73% of the displacements were due to neutrons below 20 MeV, 25% due to neutrons between 20 and 150 MeV, and only 2% above 150 MeV [7].

In Method 2, the damage cross-sections are not explicitly determined and no synthetic sample is assumed. Instead, MCNPX is run and the target specified in the input file is a model of the actual target or a reasonable approximation of it. Also, the proton source profile for the target as in Fig. 3 is used. A tally volume is specified, and the number of displacements (or the average damage energy), helium atoms, or hydrogen atoms per incident proton is provided in the output. For our Method 2 calculations, the tally volume consisted of the volume of intersection of the outer shell near the tip and a cone whose point is at point O in Fig. 2 and whose axis extends downward in the $-Z$ direction. The cone angle is 3° and the tally volume is 0.0705 cm³. At present, information is not readily available concerning how much of the damage obtained by Method 2 is due separately to protons and neutrons or how the damage depends on the energies of the protons and neutrons producing the damage. Also, Method 2 requires greater computer capacity than Method 1. Method 2 does have the advantage, however, that it provides a more accurate

simulation of the geometry of the actual target. This may be particularly useful for calculations of hydrogen production and retention, as is discussed below.

4.2. Displacement cross-sections and production rates

We ran LAHET for 570 MeV protons on aluminum and obtained a displacement cross-section of 825 barns assuming a threshold displacement energy of 27 eV. As indicated above, the peak proton flux at the center of the entrance window is 1.56×10^{14} protons/cm^{2}s per mA, which gives a displacement production rate of 4.1 dpa/yr per mA due to protons.

For the displacement cross-sections due to neutrons, we ran SPECTER for energies below 20 MeV, downloaded the LA150 information for energies from 20 to 150 MeV, and ran LAHET for energies from 150 to 570 MeV. These cross-sections were then fitted to the same bin structure as shown by the fitted points for the differential neutron flux in Fig. 6. The result is shown in Fig. 8. Then, the cross-sections and fluxes were multiplied bin-by-bin, thus obtaining the displacement rates in bin. The resulting fraction, F, of displacements due to neutrons with energies above E is shown as a function of neutron energy E in Fig. 9. The total displacement rate due to neutrons was about 0.47 dpa/yr per mA. As can be seen in Fig. 9, the contribution due to neutrons below 20 MeV comprised about 80%, due to neutrons between
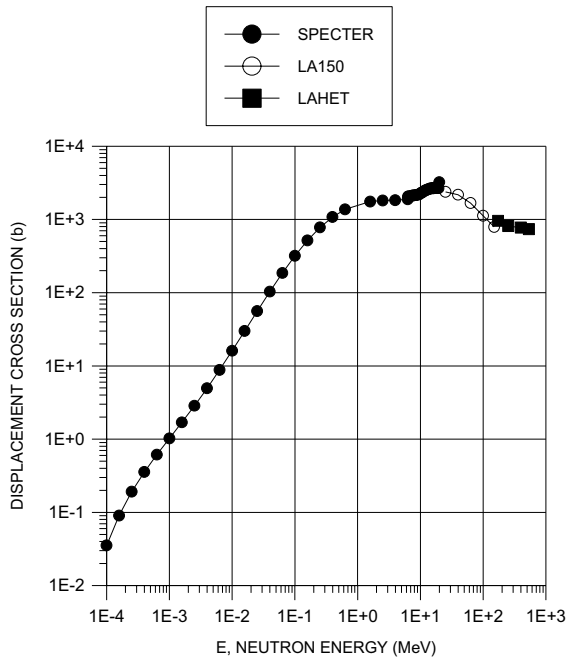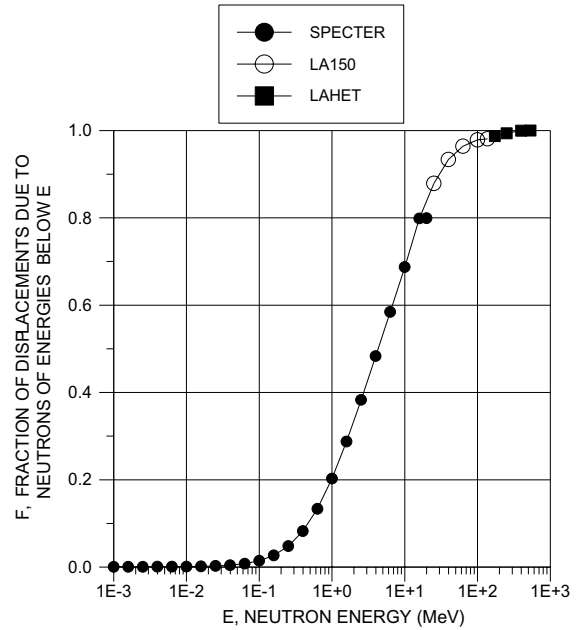

Fig. 9. Fraction, F, of displacements due to neutrons of energies below E versus neutron energy E. $F = 1$ corresponds to displacement production rate of 0.47 dpa/yr per mA. Tip of the SINQ entrance window.

20 and 150 MeV about 18%, and above 150 MeV about 2%. These percentages are quite similar to those observed for SNS, as mentioned above.

Thus, the proton and neutron displacement rates are calculated to be about 4.1 and 0.47 dpa/yr per mA, respectively, giving a total of 4.6 dpa/yr per mA. The displacement concentration corresponding to the total charge of 6.77 Ah delivered to the SINQ Target 3 during the STIP-I irradiation is about 3.6 dpa.

The above-mentioned total of 4.6 dpa/yr per mA can be compared with values obtained using Method 2 where the target for the calculation consisted of a model of the entire target at SINQ Target 3 or a portion of it. The results for four Method 2 models are summarized in Table 1, indicated by Method 2A, 2B, 2C, and 2D, with the number of histories (number of incident protons) given in parentheses and varying from 500,000 to 10 million (5E5 to 1E7 p's). For Methods 2A and 2B, the entire target was modeled in the input file, for Method 2C only the outer and inner hemispherical portion of the container shells and the D$_2$O between the shells and inside the inner hemisphere were included, plus two rows of rods, and for Method 2D the target was the same as for 2C but without the two rows of rods. The results indicate displacement production rates that vary from 3.6 to 4.1 dpa/yr per mA, with relative percentage errors from 5% to 20% (as shown in parentheses). As expected, the errors decrease with increasing number of incident

Fig. 8. Displacement cross-section for aluminum versus neutron energy.

Table 1
Summary of production rates and concentrations for STIP-I for displacements, He, and H

	Displacements	Helium	Hydrogen[a]
Production rate[b]	(dpa/yr per mA)	(appmHe/yr per mA)	(appmH/yr per mA)
Method 1	4.6	1000	3500
Method 2A, 5E5 p's	4.1 (20%)	1580 (40%)	4360 (20%)
Method 2B, 1E6, p's	3.6 (15%)	1480 (27%)	4170 (17%)
Method 2C, 5.5E6 p's	4.0 (6%)	1000 (13%)	3580 (8%)
Method 2D, 1E7 p's	3.8 (5%)	950 (10%)	3460 (6%)
Concentration, STIP-I	(dpa)	(appmHe)	(appmH)
Method 1	3.6	770	2700
Method 2A	3.2	1200	3400
Method 2B	2.8	1140	3200
Method 2C	3.1	770	2800
Method 2D	2.9	730	2700

[a] Retained hydrogen, based on IOPT 14.
[b] Beam current for STIP-I, 0.86 mA (Fig. 10 in [1]).

protons. The displacement concentrations for STIP-I vary from 2.8 to 3.2 dpa.

4.3. Helium cross-sections and production rates

The LAHET calculation for the He production cross-section for 570 MeV protons on aluminum gives 0.20 barns. Then, based on the center-line flux of 1.56×10^{14} protons/cm^{2}s per mA, we calculate the He production rate for protons to be 988 appmHe/yr per mA. Fig. 10 shows the cross-sections in the neutron energy ranges: (A) below 20 MeV from SPECTER, (B) from 20 to 150 MeV from LA150, and (C) above 150 MeV from LAHET. There is a large discrepancy between the LA150 and LAHET cross-sections at 150 MeV, which is discussed further below. The fraction of helium atoms due to neutrons below energy E is plotted versus neutron energy E in Fig. 11. We see that the neutrons begin to produce helium above about 6 MeV. The fractional amounts of helium produced in ranges (A), (B), and (C) are about 38%, 55%, and 7%, respectively. The total He production rate due to neutrons is about 13 appmHe/yr per mA. Adding this to the 988 appmHe/yr per mA due to protons, we obtain a total of about 1000 appmHe/yr per mA using Method 1. The corresponding helium production for the STIP-I irradiation delivering 6.77 Ah of proton charge is 770 appmHe. These production rates are shown in Table 1.

The results using Method 2 gave production rates ranging from 950 to 1580 appmHe/yr per mA (Table 1). The corresponding rates for the STIP-I experiment range from 730 to 1200 appmHe (Table 1).

LAHET and MCNPX offer two tally options for obtaining information concerning production of gas atoms. Option IOPT 3 tallies the particles where they are produced, and IOPT 14 tallies them where they come to
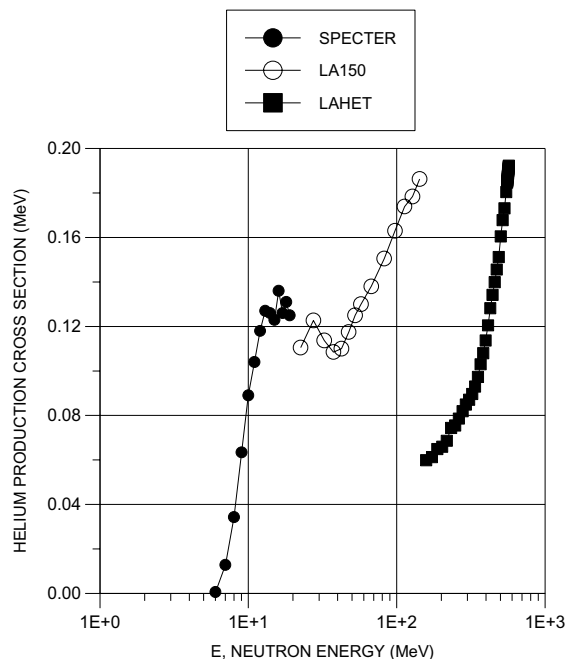

Fig. 10. Helium production cross-section versus neutron energy.

rest. Thus, He atoms that escape the target are counted for IOPT 3 but not for IOPT 14. For helium, the cross-section results from IOPT 3 and 14 were in agreement, indicating that all of the helium was retained in the irradiated sample. This is shown for 570 MeV protons on aluminum in Fig. 12.

We also did a study of the effect of varying the thickness of the synthetic sample on the LAHET-determined helium cross-sections (LAHET 2.83, one
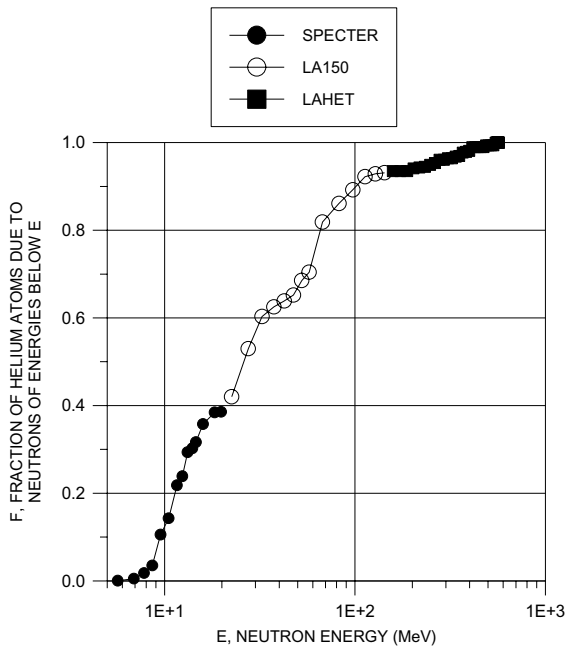
Fig. 11. Fraction, F, of helium production rate due to neutrons of energies below E versus neutron energy E. $F = 1$ corresponds to 7.0 appmHe/yr per mA.
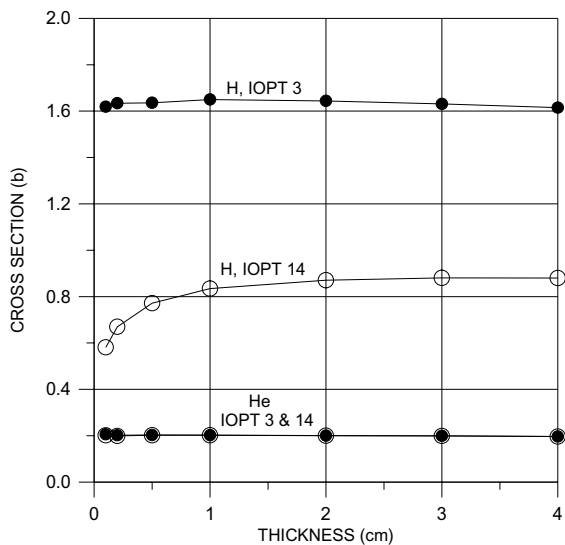

Fig. 12. Cross-section versus thickness for helium and hydrogen production using IOPT 3 and 14. LAHET 2.83, one million 570-MeV protons on aluminum, radius 1 cm.

million histories, target radius 1 cm). The results (Fig. 12) for 570 MeV protons on aluminum show no dependence on thickness.

4.4. Hydrogen cross-sections and production rates

We ran LAHET IOPT 3 and 14 for hydrogen also, and the results were quite different than for helium. As seen in Fig. 12 for 570 MeV protons on aluminum as a function of target thickness, IOPT 3 gave a rather steady cross-section of 1.64 b, which corresponds to about 8000 appmH/yr per mA. IOPT 14, however, gave about 0.6 b for a thickness of 0.1 cm, increasing with increasing thickness to a fairly steady value of about 0.87 b for targets 1–4 cm thick. This steady value corresponds to about 4300 appmH/yr per mA. However, the thickness of the outer shell of SINQ Target 3 is 0.3 cm. At this thickness, Fig. 12 indicates a hydrogen cross-section of about 0.71 b using IOPT 14, which implies a rate of 3500 appmH/yr per mA by Method 1.

Cross-sections for H production due to neutrons were obtained from SPECTER ($E < 20$ MeV), LA150 ($20 < E < 150$ MeV), and LAHET ($E > 150$ MeV) using IOPT 3 and 14. The cross-sections were folded into the fluxes as a function of neutron energy. Hydrogen rates of 35 and 32 appmH/yr per mA were obtained for IOPT 3 and 14, respectively. Thus, again the neutron rates were a small fraction of the proton rates. The total rates may still be regarded as about 8000 and 3500 appmH/yr per mA for IOPT 3 and 14, respectively. The value for IOPT 14 is regarded as the more significant one from the point of view of hydrogen remaining in the SINQ target, and thus the value of 3500 appmH/yr per mA is given in Table 1 for Method 1. The corresponding STIP-I concentration is about 2700 appmH. The Method 2 hydrogen production rates for IOPT 14 vary from 3460 to 4360 appmH/yr per mA with STIP-I concentrations of 2700 to 3400 appmH.

5. Discussion

The question arises as to the range of 570 MeV protons in aluminum. Friedlander et al. show a plot (Fig. 6-6 in [20]) of the range of protons in aluminum times the density of aluminum as a function of proton energy. For 570 MeV protons, the plot indicates 1.7×10^5 mg/cm^2, and for a density of 2.70 g/cm^3 we obtain a range of about 63 cm. Also, the stopping power for 570 MeV protons in aluminum is shown in Fig. 6-4 of [20] as about 0.002 MeV per mg/cm^2 or 5.4 MeV/cm. We conclude the decrease in energy of the incident protons during passage through the 0.3-cm-thick container shells is not a serious consideration in the present application.

In Fig. 12, the decrease observed in hydrogen cross-section for 570 MeV protons with decreasing thickness of synthetic sample below 1 cm is probably best understood in terms of the loss of protons emanating from

nuclear reactions through the plane entry and exit surfaces perpendicular to the beam direction. However, even as the thickness increases well above 1 cm these protons continue to leave through the curved transverse surface of the cylindrical target sample. The retention of helium stems from its greater stopping power, $-\mathrm{d}E/\mathrm{d}x$, which is to be expected since the well-known Bethe stopping-power expression indicates a proportionality to z^2 where z is the atomic number of the moving ion (see, for example, [20], Eq. 6-13 or 6-14). This question of hydrogen production and retention as a function of the size and shape of the target would seem to deserve greater attention. It should be pointed out, however, that the effect of hydrogen on the properties of irradiated spallation materials is further complicated by possible trapping of hydrogen by microstructural features such as small helium bubbles. Using Method 2 avoids questions about the influence of the choice of size and shape of the target used for Method 1 on the determination of cross-section. But, in Method 2 the user selects the location and dimensions of the tally volume, and more work needs to be done to clarify how best to make this selection.

The large discrepancy shown in Fig. 10 between helium cross-sections near 150 MeV for neutrons on aluminum as calculated by LA150 and LAHET is troublesome. It seems that some significant correction is required in one or both of these codes and processes. But the neutrons above 150 MeV contribute only about 2% of the helium produced as seen in Fig. 10, so the issue is not of great importance as far as radiation damage at the entrance window at SINQ is concerned.

A preliminary report has been issued [2] describing tensile tests on samples cut from the SINQ Target 3 (Mark II Type) after it received the 6.77 Ah charge of 570 MeV protons. Samples from the center section, which are calculated here to have received a dose of about 3.2 dpa as mentioned above, were tensile tested at room temperature and revealed a decrease in uniform elongation from 17% to 6.5% as a result of the irradiation. By comparison, a 5052 aluminum alloy (containing 2.5 wt% Mg and therefore similar in composition to the alloy used for the SINQ window) was irradiated with fission neutrons at 55 °C to a dose of 2.5 dpa [21]. This dpa dose is probably equal within calculational error to the calculated dose of 3.2 dpa for STIP-I. Nevertheless, the 5052 alloy experienced a decrease in uniform elongation from 20% to only 16% [21]. It is tempting, then, to attribute the lesser radiation embrittlement in the fission-neutron-irradiated material to the reduced amounts of helium and hydrogen that were produced. This is, however, a tentative explanation, since much more research needs to be done to better understand radiation damage in irradiated aluminum and its alloys.

References

[1] Y. Dai, G.S. Bauer, J. Nucl. Mater. 296 (2001) 43.

[2] Y. Dai, H. Kaiser, K. Geissmann, G.S. Bauer, R. Zumsteg, H.P. Linder, F. Gröschel, PSI Scientific and Technical Report 2000, Vol. VI, Paul Scherrer Institut, Villigen, Switzerland, 2001, p. 33.

[3] R.E. Prael, H. Lichtenstein, Report LA-LIR 89-3014, Los Alamos National Laboratory, Los Alamos NM, 1989.

[4] M. Pepin, private communication.

[5] H.G. Hughes, K.J. Adams, M.B. Chadwick, J.C. Comly, L.J. Fox, H.W. Egdorf, S.C. Frankle, J.S. Hendricks, R.C. Little, R. MacFarlane, R.E. Prael, L.S. Waters, M.C. White, P.G. Young, F.X. Gallmeier, E.C. Snow, in: Second International Topical Meeting on Nuclear Applications of Accelerator Technology (AccApp98), American Nuclear Society, La Grange Park, Illinois 60526, 1998, p. 281.

[6] J.F. Briesmeister (Ed.), Los Alamos National Laboratory. See also, Report LA-12625-M, Los Alamos National Laboratory, Los Alamos, NM, 1997.

[7] P.D. Ferguson, M.S. Wechsler, L.K. Mansur, K. Farrell, M.W. Wendel, in: Proceedings, Embedded Topical Meeting on Accelerator-Driven Transmutation Technology and Applications, Reno, Nevada, 11–15 November 2001. To be published by American Nuclear Society.

[8] L.R. Greenwood, R.K. Smither, ANL/FPP/TM-197, January 1985.

[9] M.S. Wechsler, D.R. Davidson, L.R. Greenwood, W.F. Sommer, in: F.A. Garner, J.S. Perrin (Eds.), Effects of Radiation on Materials: Twelfth International Symposium, STP 870, American Society for Testing and Materials, Philadelphia, 1985, p. 1189.

[10] M.S. Wechsler, C. Lin, W.F. Sommer, in: E.D. Arthur, A. Rodriguez, S.O. Schriber (Eds.), Proceedings of the International Conference on Accelerator-Driven Transmutation Technologies and Applications, Las Vegas, NV, July 1994, AIP Conference Proceedings 346, American Institute of Physics, Woodbury, New York, 1995, p. 466.

[11] M.S. Wechsler, C. Lin, W.F. Sommer, L.L. Daemen, P.D. Ferguson, in: Proceedings of the Symposium on Radiation Materials Science in Technology Applications, Anaheim, California, 4–8 February 1996, J. Nucl. Mater. 244 (1997) 177.

[12] M.S. Wechsler, C. Lin, P.D. Ferguson, L.K. Mansur, W.F. Sommer, in: Proceedings of the Second International Conference on Accelerator-Driven Transmutation Technologies and Applications, held in Kalmar, Sweden, 3–7 June 1996, Vol. 2, Editor, Henri Condé, Upsala University, 1997, p. 968.

[13] M.S. Wechsler, M.H. Barnett, D.J. Dudziak, R.K. Corzine, W.F. Sommer, E.J. Pitcher, P.D. Ferguson, L.K. Mansur, K. Farrell, L.A. Charlton, J.M. Barnes, J.O. Johnson, in: Proceedings of the Topical Meeting on

Nuclear Applications of Accelerator Technology, American Nuclear Society, La Grange Park, Illinois, 1997, p. 21. (ANS Embedded Topical Symposium on Nuclear Applications of Accelerator Technology held in Albuquerque, New Mexico, on 16–20 November 1997).

[14] M.S. Wechsler, in: Proceedings, Second International Workshop on Spallation Materials Technology (Ancona, Italy, 19–22 September 1997), Juel-3450, Forschungszentrum Juelich, 1997. Also, European Spallation Source Report ESS-97-67-T, p. 161.

[15] M.S. Wechsler, M.H. Barnett, D.J. Dudziak, L.K. Mansur, L.A. Charlton, J.M. Barnes, J.O. Johnson, in: Materials for Spallation Neutron Sources, The Minerals, Metals, and Materials Society (TMS), Warrendale, PA, 1998, p. 23 (Proceedings of the Symposium on Materials for Spallation Neutron Sources, Orlando, Florida, 9–13 February 1997).

[16] E.J. Pitcher, P.D. Ferguson, G.J. Russell, R.E. Prael, D.G. Madland, J.D. Court, L.L. Daemen, M.S. Wechsler, in: Materials for Spallation Neutron Sources, The Minerals, Metals, and Materials Society (TMS), Warrendale, PA, 1998, p. 15 (Proceedings of the Symposium on Materials for Spallation Neutron Sources, Orlando, Florida, 9–13 February 1997).

[17] M.H. Barnett, M.S. Wechsler, D.J. Dudziak, R.K. Corzine, L.A. Charlton, L.K. Mansur, in: Proceedings, Third International Topical Meeting on Nuclear Applications of Accelerator Technology (AccApp99), American Nuclear Society, La Grange Park, Illinois, 1999, p. 555. (ANS Winter Meeting, Long Beach, CA, 14–18 November 1999).

[18] M.B. Chadwick, H.G. Hughes, R.C. Little, E.J. Pitcher, P.G. Young, Progr. Nucl. Energy 38 (1–2) (2001) 179.

[19] P.G. Young, E.D. Arthur, M.B. Chadwick, in: A. Gandini, G. Reffo, (Eds.), Proceedings of the IAEA Workshop on Nuclear Reaction Data and Nuclear Reactors – Physics, Design, and Safety, World Scientific, 1998, p. 227.

[20] G. Friedlander, J.W. Kennedy, E.S. Macias, J.M. Miller, Nuclear and Radiochemistry, John Wiley, New York, 1981.

[21] K. Farrell, J. Nucl. Mater. 97 (1981) 33.